

RESEARCH ARTICLE

10.1002/2016SW001376

Key Points:

- Latitudinal distribution of GMDs varies with Dst
- GMD magnitudes can vary strongly at fixed latitude
- Statistical likelihood of large GMDs is nearly independent of storm strength at high latitudes

Supporting Information:

- Supporting Information S1
- Data Set S1

Correspondence to:

J. R. Woodroffe,
jesse.woodroffe@gmail.com

Citation:

Woodroffe, J. R., S. K. Morley, V. K. Jordanova, M. G. Henderson, M. M. Cowee, and J. G. Gjerloev (2016), The latitudinal variation of geoelectromagnetic disturbances during large ($D_{st} \leq -100$ nT) geomagnetic storms, *Space Weather*, 14, doi:10.1002/2016SW001376.

Received 10 FEB 2016

Accepted 16 AUG 2016

Accepted article online 20 AUG 2016

The latitudinal variation of geoelectromagnetic disturbances during large ($D_{st} \leq -100$ nT) geomagnetic storms

J. R. Woodroffe¹, S. K. Morley¹, V. K. Jordanova¹, M. G. Henderson¹, M. M. Cowee¹, and J. G. Gjerloev^{2,3}
¹Space Science and Applications, Los Alamos National Laboratory, Los Alamos, New Mexico, USA, ²Applied Physics Laboratory, The Johns Hopkins University, Laurel, Maryland, USA, ³Birkeland Centre for Space Science, University of Bergen, Bergen, Norway

Abstract Geoelectromagnetic disturbances (GMDs) are an important consequence of space weather that can directly impact many types of terrestrial infrastructure. In this paper, we analyze 30 years of SuperMAG magnetometer data from the range of magnetic latitudes $20^\circ \leq \lambda \leq 75^\circ$ to derive characteristic latitudinal profiles for median GMD amplitudes. Based on this data, we obtain a parameterization of these latitudinal profiles of different types of GMDs, providing an analytical fit with D_{st} -dependent parameters. We also obtain probabilistic estimates for the magnitudes of “100 year” GMDs, finding that $\dot{B} = 6.9$ (3.60–12.9) nT/s should be expected at $45^\circ \leq \lambda < 50^\circ$, exceeding the 5 nT/s threshold for dangerous inductive heating.

1. Introduction

One of the most important consequences of space weather is the generation of geoelectromagnetic disturbances (GMDs) that can directly affect terrestrial infrastructure [National Research Council Committee on the Societal and Economic Impacts of Severe Space Weather Events, 2008]. Because of their particular ground-level effects, three types of GMD are of greatest concern: magnetic perturbations (ΔB), which result from transient changes in the total magnitude of the horizontal component of the geomagnetic field; magnetic time variations (\dot{B}), which are a quantification of the instantaneous rate of change of the horizontal geomagnetic field vector; and geoelectric fields (E), which have a complicated dependence on both the local ground conductivity and the spatiotemporal variations of the magnetic field. Each type of GMD affects different types of infrastructure: ΔB interferes with magnetic direction finding (used in surveying and drilling) [Reay et al., 2005; Watermann et al., 2006]; \dot{B} causes heating of electrical components (such as transformers) and the triggering of power grid irregularities [Boteler et al., 1998]; and E is responsible for driving geomagnetically induced currents (GICs) in long conductors such as pipelines, railways, and power lines [Ptitsyna et al., 2008; Viljanen et al., 2010; Eroshenko et al., 2010; Marshall et al., 2010; Viljanen et al., 2012, 2014].

Just as earthquake-prone areas must account for the possibility of extreme seismic events, infrastructure with known space weather vulnerabilities needs to be designed to withstand a range of severe geomagnetic conditions. At present, there appears to be a consensus that critical infrastructure must be prepared for a 1 in 100 year (“100 year”) GMD event [see, e.g., National Research Council Committee on the Societal and Economic Impacts of Severe Space Weather Events, 2008; Natural Environment Research Council (NERC) Geomagnetic Disturbance (GMD) Task Force, 2015]. Moreover, due to a growing recognition of the potentially devastating societal impacts that could result from a severe GMD event [e.g., Hapgood, 2010], understanding GMD variability has become an important issue for policy makers as well as scientists: as part of its National Space Weather Action Plan, the White House has recently called for establishing 100 year geoelectric field benchmarks (<https://www.whitehouse.gov/blog/2015/10/28/enhancing-national-preparedness-space-weather-events>).

Although historical records contain magnetic observations spanning more than 100 years, the time resolution of this historical data is often unsuitable for GMD analyses. As a consequence, it is necessary to extrapolate from shorter data sets to estimate the severity of a 100 year GMD event. A variety of efforts have been undertaken in this direction, frequently using data from the well instrumented European magnetometer arrays. For example, Pulkkinen et al. [2012] used IMAGE magnetometer data (from 23 stations in $55^\circ \leq \lambda \leq 75^\circ$, where λ is the geomagnetic latitude or magnetic latitude (MLAT) [Hapgood, 1992]) from 1993 to 2006 to extrapolate

the amplitude of a 100 year geoelectric field perturbation, and *Viljanen et al.* [2001] used data from the IMAGE magnetometer array ($60^\circ \leq \lambda \leq 78^\circ$) for the period of 1983–2000 to study the magnitude and spatial distribution of \dot{B} in Fennoscandia. Perhaps the most comprehensive study of European GMDs was performed by *Thomson et al.* [2011], who analyzed data from 28 different stations during 1979–2006 using extreme value theory to in order to estimate the magnitude of 100 year GMDs, finding that $\Delta B \approx 2000\text{--}5000$ nT and $B \approx 16\text{--}66$ nT/s are expected at latitudes of $55^\circ \leq \lambda < 60^\circ$ in Europe.

Despite the obvious benefits of using European magnetometer data (namely, excellent spatial and temporal resolution), these data only represent a small fraction of what is available globally. Thanks in large part to two recent initiatives, INTERMAGNET [Love, 2013] and SuperMAG [Gjerloev, 2012], data from distributed global networks of magnetometers have become easily accessible and it is now possible to extend GMD analyses to larger, more geographically diverse data sets than ever before. For example, *Ngwira et al.* [2013] used the INTERMAGNET data set to study the spatial distribution of GMDs during $Dst < -245$ nT geomagnetic storms from 1989 to 2012 (a total of 12 events); using this larger data set, they were able to confirm the ubiquity of a “latitude threshold” for GMD amplitudes that had been first suggested by *Pulkkinen et al.* [2012].

An implicit assumption among studies that focus on large Dst events [e.g., *Ngwira et al.*, 2013; *NERC GMD Task Force*, 2015] is that the largest GMDs will occur during the most intense storms. On the face of it, this is not unreasonable—after all, it is geomagnetic activity that provides energy for the physical processes that are ultimately responsible for producing GMDs, so more intense activity should drive GMD production more strongly. However, the large-scale current systems associated with global storm dynamics are usually not responsible for generating the most intense GMDs; instead, smaller-scale magnetospheric dynamics are believed to drive localized ionospheric currents that are in turn responsible for generating large ground signatures [Viljanen et al., 2001]. The relationship between Dst and GMD magnitudes is not well characterized at present, as studies have tended to focus on a few extreme events (such as the 1989 “Québec” storm and the 2003 “Halloween” storm) [e.g., *Pulkkinen et al.*, 2012; *Wei et al.*, 2013].

In this paper, we present the largest statistical analysis of GMD amplitudes to date, using data from the SuperMAG collaboration to expand on the prior work of *Ngwira et al.* [2013] and characterize latitudinal variation of GMDs (ΔB , \dot{B} , and E) during all $Dst \leq -100$ geomagnetic storms from 1981 to 2011. Using this data set, we derive profiles for the latitudinal distribution of GMD amplitudes as a function of Dst . Then, by characterizing the probability distribution of GMD amplitudes as a function of MLAT, we will extract properties of the distribution and estimate 100 year GMD amplitudes as a function of both storm strength and geomagnetic latitude.

2. Data Set

A geomagnetic storm is commonly defined as any period during which the Dst index decreases below -30 nT [Gonzalez et al., 1994]. Storms with more negative Dst are often separated into additional categories, for example, *Loewe and Prölss* [1997] have defined five different classes of storm: weak ($Dst > -50$ nT); moderate ($-50 \geq Dst > -100$ nT); strong ($-100 \geq Dst > -200$ nT); severe ($-200 \geq Dst > -350$ nT); and great ($Dst \leq -350$ nT). For our study, we chose to separate the storms into four classes based on Dst : weak-moderate ($Dst > -100$ nT); strong ($-100 \geq Dst > -200$ nT); severe ($-200 \geq Dst > -300$ nT); and extreme ($Dst \leq -300$ nT). We follow the convention that the minimum Dst for any event to be classified as a storm is -30 nT, but as noted above, we are only analyzing data from storms in the latter three categories. The departure of our classification scheme from that of *Loewe and Prölss* [1997] is physically motivated: since Dst is theoretically proportional to the energy stored in the ring current [Sckopke, 1966], equal divisions of Dst should correspond to equal amounts of stored energy (e.g., a storm with $Dst = -200$ nT has nominally twice as much stored energy as one with $Dst = -100$ nT).

For this study, we obtained 1 min baseline-subtracted magnetometer data in geomagnetic NEZ coordinates (where N is north-south, E is east-west, and Z is locally vertical) from the SuperMAG database [Gjerloev, 2012] for all $Dst \leq -100$ nT geomagnetic storms between the years of 1981–2011 (a total of 218 events). For each storm, we considered all geomagnetic longitudes but only used data from stations with $20^\circ \leq \lambda \leq 75^\circ$. Figure 1 shows the change in station availability over time, with Figure 1a illustrating latitudinal coverage over the 30-year period of this study, and Figure 1b shows the overall number of stations during each storm (regardless of latitude) and the yearly mean sunspot number.

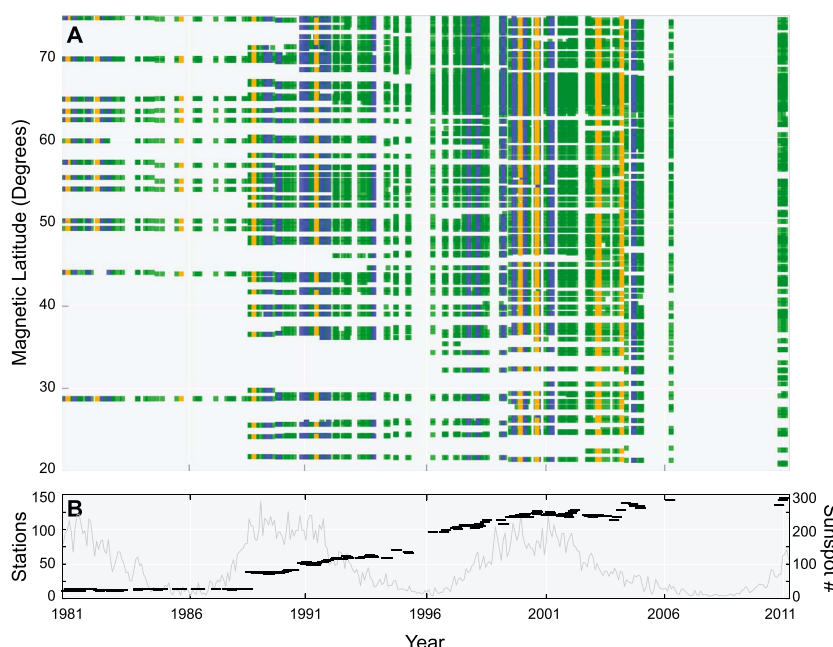


Figure 1. Coverage and availability of magnetometer stations during this study. (a) Latitudinal coverage of magnetometer stations during each storm; (b) total number of stations with data during each storm. In Figure 1a, strong storms are shown in green, severe storms are shown in blue, and extreme storms are shown in orange. Note that coverage is only shown for storm time intervals; magnetometer locations during periods without $Dst \leq -100$ nT are not indicated nor are inactive magnetometers during storm time intervals. Periods without any color across the entire range of magnetic latitude (such as occurred between 2007–2011) did not have any geomagnetic storms with $Dst \leq -100$ nT. In Figure 1b, the yearly mean sunspot number is plotted in gray, illustrating the solar cycle coverage of our data set.

When a period of geomagnetic activity contained multiple distinct intervals with $Dst \leq -100$ nT, we applied the 80% recovery criterion of Halford et al. [2010] to separate individual storms. During particularly complex periods of geomagnetic activity (e.g., March 1989), solar wind data were used to determine if particular active periods were associated with distinct drivers. In one case, July 2004, multiple distinct solar wind drivers were identified but the resultant sequence of three $Dst < -100$ nT intervals was treated as a single storm because the atypically large GMDs during the third interval suggested that the magnetosphere had not returned to prestorm conditions despite the recovery of Dst . A complete listing of storm intervals used in this study is available as an electronic supplement.

Of the 218 storms present in this data set, 182 were classified as strong, 26 as severe, and 10 as extreme. For each station during each storm, we calculated time series of ΔB , \dot{B} , and E . Temporal data gaps of any duration were filled using linear interpolation, since this method introduces neither spurious peaks nor sharp discontinuities (the presence of a prolonged data gap during the peak of a storm might occasionally result in anomalously low peak values, but no peaks will be introduced by the interpolation). We calculated ΔB from the horizontal components of the ground magnetic fields, $\Delta B = \sqrt{B_N^2 + B_E^2}$; \dot{B} was calculated from the time derivative (obtained using Fourier spectral methods) of the horizontal magnetic fields, $\dot{B} = \sqrt{\dot{B}_N^2 + \dot{B}_E^2}$; and E was calculated using a one-dimensional, normally incident plane wave method [see, e.g., Cagniard, 1953; Wait, 1958] that made use of the six-layer Québec ground conductivity profile (QUE6) [see Boteler, 2015, Figure 1]. It should be noted that we are using a single representative conductivity profile because depth-resolved conductivity measurements are only available in limited regions (notably Europe) [see, e.g., Ádám et al., 2012; Viljanen et al., 2012]; in the absence of good local measurements, previous studies have adopted the Québec profile as a representative model [Pulkkinen et al., 2012; Ngwira et al., 2013]. Our data set was compiled from the largest GMD of each type (ΔB , \dot{B} , E) at each station during each storm (the peaks of different types of GMD need not have been simultaneous).

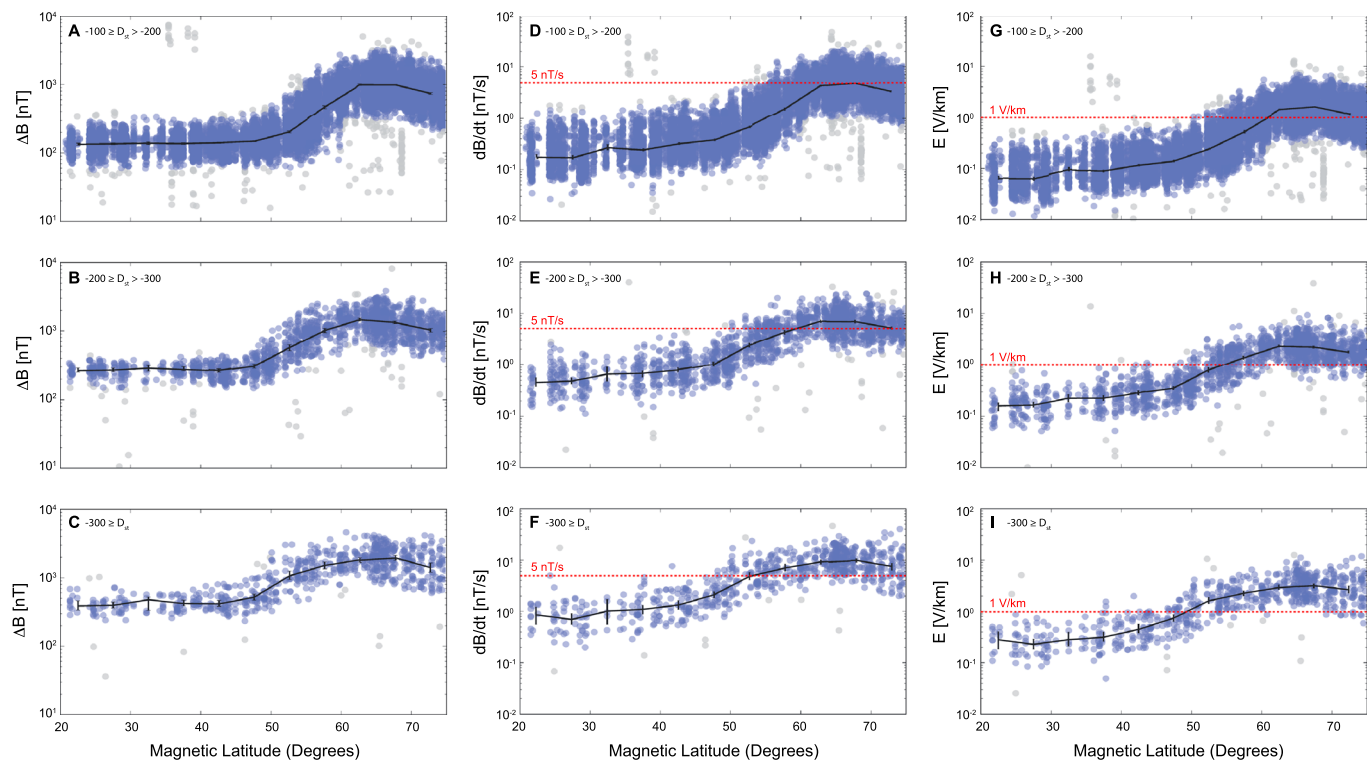


Figure 2. Latitudinal dependence of GMD amplitudes. (a–c) ΔB for strong, severe, and extreme storms; (d–f) \dot{B} for strong, severe, and extreme storms; (g–i) E (calculated using the QUE6 conductivity profile) for strong, severe, and extreme storms. In each panel, individual maxima from different stations are shown as a blue circle; the concentration of points is indicated by the darkness of the circles. Also in each panel, the median GMD amplitude (with 95% CI) is plotted with a solid black line. Points shaded in gray are those excluded by a MADLOG(4) filter. In Figures 2d–2i, established GMD hazard levels are indicated with dashed red lines.

3. Results and Discussion

In the storm time magnetosphere, there are multiple current systems that are active on different spatiotemporal scales (e.g., Chapman-Ferraro currents, ring current, and ionospheric electrojets) [see, e.g., Kamide and Kokobun, 1996; Ganushkina et al., 2015]. In some cases, there is a well-known relationship between certain types of GMDs and dynamics of particular current systems, such as Chapman-Ferraro currents and sudden commencements [Kappenman, 2003; Shinbori et al., 2009], but there are usually multiple current systems contributing simultaneously, preventing the attribution of GMDs to specific sources.

Another issue is that magnetospheric current systems (such as the ring current and electrojets) are known to exhibit characteristic magnetic local time (MLT) variations [Rostoker and Phan, 1986; Le et al., 2004; Tomita et al., 2011; Newell and Gjerloev, 2012; Guo et al., 2014], and this variability is likely to be important during individual storms. Owing to the statistical nature of the present study, we are justified in disregarding explicit MLT dependence by the simple fact that a location is just as likely to be at noon as at midnight during any given storm. The effects of MLT dependence are not absent from our results, however, as it manifests as a source of variability in GMD magnitude at fixed MLAT.

3.1. Latitudinal Variation

In Figure 2, the peak GMD amplitudes from all stations during all storms are plotted as a function of latitude and storm strength, with each peak GMD from a given station marked by a semitransparent circles (darker colors indicate a concentration of data points, while gray indicates that the point is excluded from analysis by filtering as discussed in Appendix A). Figures 2a–2c show the peak ΔB measured during strong (Figure 2a), severe (Figure 2b), and extreme (Figure 2c) storms; Figures 2d–2f similarly show the peak values of \dot{B} and panels Figures 2g–2i show the peak values of E . In Figures 2d–2f and Figures 2g–2i, established hazard levels (5 nT/s and 1 V/km) are indicated with dashed red lines.

The latitudinal distribution of GMD magnitudes is qualitatively similar in each case, with the lowest values occurring at the low MLAT and the largest values occurring at high (but not the highest) MLAT. As Figure 2

Table 1. Fitting Parameters for Equation (1) Applied to ΔB

Dst Range (nT)	α	β	γ	λ_0	$\Delta\lambda$
$-200 < Dst \leq -100$	2.14	3.34	1.86	58.2	5.8
$-300 < Dst \leq -200$	2.43	3.40	1.30	55.5	6.5
$Dst \leq -300$	2.61	3.41	0.67	52.9	6.2

shows, there is significant variation (as much as a factor of 10) in observed peak GMDs at all latitudes. This variability arises from a combination of factors including the previously mentioned MLT dependence, differences in storm strength, and intrinsic stochasticity of storm time current systems.

3.1.1. Characterization of Median GMDs

Before addressing the variability of peak GMDs at a given MLAT, we would like to have a baseline model for peak GMDs. In order to derive this model, we partitioned the data sets shown in Figure 2 into 5° latitudinal bins (e.g., $20^\circ - 25^\circ$, ..., $70^\circ - 75^\circ$). We then applied a MADLOG(4) filter (see Appendix A) to the data and found the median of the remaining values; 1000 applications of the bootstrap resampling method [Efron and Tibshirani, 1986; Press et al., 1992] were then used to obtain a 95% confidence interval (CI) on the median. These values are shown as black lines with error bars in Figure 2.

As these results show, typical peak GMD magnitudes increase with both with MLAT and storm strength (decreasing Dst). The latitudinal distributions of ΔB , \dot{B} , and E are qualitatively similar, although ΔB flattens out more strongly at low latitudes. The latitudinal variation suggests that there are (at least) two different sources for ΔB : a relatively small-amplitude source that is effective at low MLAT and a stronger source at high MLAT. The fact that ΔB asymptotes more quickly than either \dot{B} or E at low MLAT suggests that these GMDs may be driven by different processes and may also indicate that the spectral content of GMDs (which both depend on time variations) has MLAT dependence.

What are the consequences of these typical GMDs? An oft-cited threshold for magnetic induction hazards is $\dot{B} = 5$ nT/s [e.g., Molinski et al., 2000; Boteler, 2001]. As shown in Figures 2 and 2e, this value is frequently exceeded by storms with $Dst \leq -200$ nT, particularly for $60^\circ \leq \lambda \leq 70^\circ$ but also at lower latitudes during extreme storms. Similarly, the $E = 1$ V/km threshold for “extreme” geoelectric fields [NERC, 2015; Ngwira et al., 2015] is below the median E for extreme storms and is frequently exceeded during strong and severe storms at $\lambda \geq 50^\circ$. The variability of GMD amplitudes and the magnitude of 100 year GMDs will be addressed in section 3.2.

3.1.2. Analytical Fitting

As mentioned above, our lack of explicit knowledge regarding the global structure of magnetospheric current systems means that we cannot obtain an explicit physical model of GMD distribution (using, e.g., Biot-Savart integration). It is nevertheless desirable to have an analytical expression for the latitudinal distribution of GMDs, as this makes it easier to extract quantitative information. Since GMD values can span more than an order of magnitude, it is convenient to instead model the logarithm of GMD magnitude. Based on the medians in Figure 2, which have a relatively constant value at low latitudes, an intermediate transition region, and a linear decrease at high latitudes, we have found that a five-parameter combination of elementary functions can provide an excellent fit to all of the observed profiles. In particular, we have found that the latitudinal distribution of the logarithm of GMD amplitudes can be well approximated by

$$\log_{10} \text{GMD} = \alpha + \Theta(\beta - \alpha - \gamma \sin(\lambda - \lambda_0)) \quad (1)$$

where Θ is a transition function,

$$\Theta(\lambda; \lambda_0, \Delta\lambda) = \frac{1}{2} \left(1 + \tanh \left(\frac{\lambda - \lambda_0}{\Delta\lambda} \right) \right) \quad (2)$$

and α , β , γ , λ_0 , and $\Delta\lambda$ are fitting parameters that must be determined for each type of storm.

Although number of parameters in our model might be regarded as large (Von Neumann is reputed to have said that five parameters is sufficient to fit an elephant and make it wiggle its trunk [Dyson, 2004]), it is the minimum required to fit the observed morphology (one for the low latitude region, two for the transition, and two for the high latitudes). The fitting parameters for our data are given in Tables 1–3, and the resulting curves are plotted in Figure 3.

Table 2. Fitting Parameters for Equation (1) Applied to \hat{B}

Dst Range (nT)	α	β	γ	λ_0	$\Delta\lambda$
$-200 < Dst \leq -100$	-0.71	2.10	9.25	65.0	12.6
$-300 < Dst \leq -200$	-0.30	1.65	3.41	58.2	12.0
$Dst \leq -300$	-0.11	1.45	1.62	53.3	11.4

Although the above fits are not physically motivated, the parameters of these fits directly reflect physical properties of the system (these properties are of course represented in the original data, but the fit provides a convenient quantification). For example, when ΔB is fit using equation (1), the asymptotic value at low latitudes (α) can be identified as the median $|Dst|$ of all the storms in the sample. To the extent that the high-latitude GMDs can be associated with electrojet currents, the decrease of the transition latitude, λ_0 , with Dst reflects the fact that the auroral oval moves equatorward during more intense storms. This equatorward movement of the auroral oval during storms was quantified by *Starkov and Feldstein* [1967], who found that the location of the auroral oval during geomagnetic storms could be described by the formula

$$\lambda_0 = 74.9^\circ - 8.6 \log_{10} |Dst| \quad (3)$$

which gives us $\lambda_0 = 57.7^\circ$ for $Dst = -100$ nT, 55.1° for $Dst = -200$ nT, and 53.2° for $Dst = -300$ nT; these values are consistent with λ_0 from Table 1. These results are also in line with a theoretical study by *Schulz* [1997], whose analytical model suggested that the auroral oval should move equatorward by 2° – 3° per 100 nT decrease in Dst .

3.1.3. The Effect of Conductivity Profile

As mentioned above, all of our analysis to this point has used the QUE6 conductivity profile of *Boteler* [2015] for calculating geoelectric fields. However, the consequences of this choice are not immediately clear. After all, many observations did not occur in regions with Québec-like geological profiles. In order to better understand how our choice of conductivities could potentially affect our results, we have performed a case study of geoelectric field variability for the 22–29 July 2004 storm event.

There were time series available from 113 different stations available for our chosen event. Using the magnetic field data from each station, we used the magnetotelluric method to calculate the geoelectric fields using 22 different conductivity profiles (21 profiles for different physiographic regions of the continental United States taken from *Fernberg* [2012] as well as QUE6). We then aggregated the data from all stations in 1° latitudinal bins and determined the minimum, maximum, and median peak geoelectric fields. In Figure 4a, the median of all peak geoelectric fields is shown in blue and the median of geoelectric fields calculated using QUE6 in orange; the range of all peak geoelectric fields in each latitudinal bin is indicated by gray error bars. The QUE6 results are further contextualized by Figure 4b, which shows the probability of the values calculated using QUE6 occurring in a given percentile range at each station. Finally, Figure 4c shows the probability distribution of the ratio of the largest calculated geoelectric field to the smallest calculated geoelectric field for each station.

Our choice of using QUE6 means that our calculated geoelectric fields are larger than would probably be calculated if one were to just choose a profile at random, as values calculated using QUE6 typically occur near the 80th percentile (i.e., fields calculated using QUE6 are typically larger than those calculated using 16 of the other 21 conductivity profiles). The actual conductivity profile that gives the largest geoelectric fields is dependent on the spectral content of each time series and varies from station to station; however, as shown in Figure 4c, the largest geoelectric fields calculated for a given time series are typically 6 times larger than the smallest (red line), while the geoelectric fields calculated using QUE6 are typically 4 times larger than the smallest. Thus, based on the results of this case study, geoelectric fields might be anywhere from 75% smaller to 50% larger than the quoted values, depending on the local conductivity profile. Use of the QUE6

Table 3. Fitting Parameters for Equation (1) Applied to E (Calculated Using the QUE6 Conductivity Profile)

Dst Range (nT)	α	β	γ	λ_0	$\Delta\lambda$
$-200 < Dst \leq -100$	-1.14	1.59	9.37	65.6	12.9
$-300 < Dst \leq -200$	-0.78	1.21	3.60	58.9	12.8
$Dst \leq -300$	-0.61	0.69	0.64	50.2	10.0

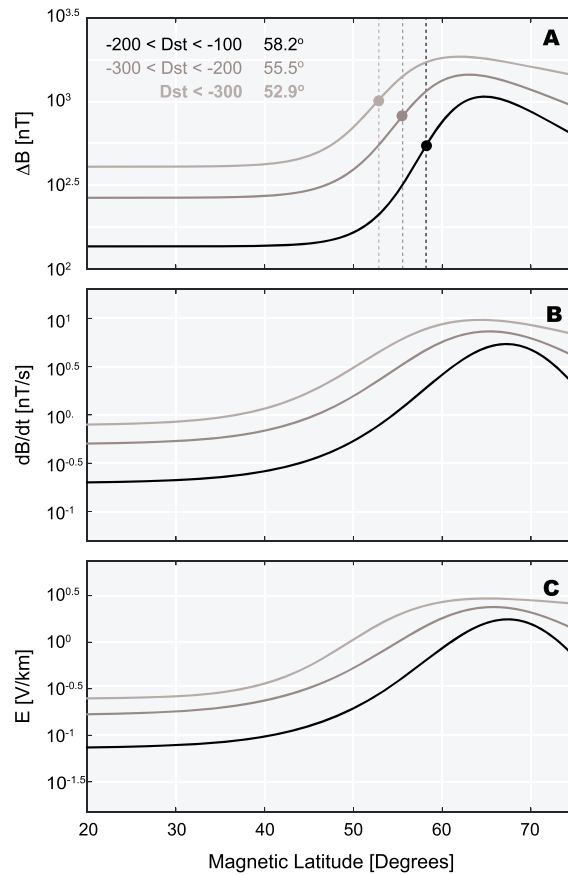


Figure 3. Analytical fits to median GMD values as a function of latitude. (a) ΔB ; (b) \dot{B} ; and (c) E (calculated using QUE6 conductivity profile). In each panel, fits for $-100 \text{ nT} \geq Dst > -200 \text{ nT}$ are shown in black, while those for $-200 \text{ nT} \geq Dst > -300 \text{ nT}$ are shown in dark gray, and those for $Dst \leq -300 \text{ nT}$ are shown in lighter gray. In Figure 3a, the center of the transition region is indicated on each curve by a shaded circle, and the latitude of this transition is indicated by a vertical dashed line.

ested should be describable by an “extreme value distribution.” As noted by *Ghil et al.* [2011], the distribution of peak values drawn from a relatively broad class of distributions (e.g., normal, lognormal, and exponential) can be modeled using the generalized extreme value distribution (GEVD). The GEVD is a three-parameter distribution (with location parameter μ , scale parameter σ , and shape parameter ξ) that is given by [*Ghil et al.*, 2011]

$$G(x; \mu, \sigma, \xi) = \frac{1}{\sigma} \left(\left(1 + \frac{x - \mu}{\sigma} \xi \right)^{-1/\xi} \right)^{\xi+1} \exp \left(- \left(1 + \frac{x - \mu}{\sigma} \xi \right)^{-1/\xi} \right) \quad (4)$$

where $\sigma > 0$.

Figure 5 shows estimated probability density functions (PDFs) of GMDs in the different latitudinal bins described in section 3.1.1, including both normalized histograms (a common nonparametric PDF estimator whose bins were determined using the Freedman-Diaconis rule [*Freedman and Diaconis*, 1981]) and best fit GEVDs (with μ , σ , and ξ determined using maximum-likelihood estimation). Figure 5 demonstrates that the GEVD often provides an excellent fit to the data, particularly for the strong and severe storms; extreme storms are less clear, owing to the relative paucity of data available for such storms. However, given that we do not have an a priori reason to expect the physical mechanisms of GMD production to change during extreme storms, we can regard the goodness of fit for the strong and severe storms to support the use of this method

profile typically results geoelectric fields that are comparable to those obtained using conductivity profiles for the American Midwest [*Fernberg*, 2012’s SU-1 and IP-1] and often yields smaller geoelectric fields than conductivity profiles corresponding to the American East Coast (*Fernberg* [2012]’s CP-1 and PT-1).

3.2. Extreme Value Analysis of Latitudinally Binned GMDs

3.2.1. The Block Maximum Method

Since we do not know the parent distribution (e.g., normal and lognormal) of GMD magnitudes during storms, it is not immediately obvious what model should be used for the distribution of peak GMDs. There are reasonable arguments to be made that GMDs should follow a lognormal distribution, based on the multiscale physical processes [*Limpert*, 2001], and authors have convincingly shown that certain geomagnetic and GMD-associated quantities can be well modeled using lognormal distributions. For example, *Danskin and Lotz* [2015] have shown that hourly ranges of ΔB are lognormally distributed; *Love et al.* [2015] demonstrated that Dst is itself well modeled by a lognormal distribution; and *Pulkkinen et al.* [2012] estimated 100 year geoelectric field magnitudes using extrapolation from a lognormal distribution.

Despite the successes of the lognormal approach in previous studies, there are compelling theoretical reasons to expect that the peak GMDs in which we are inter-

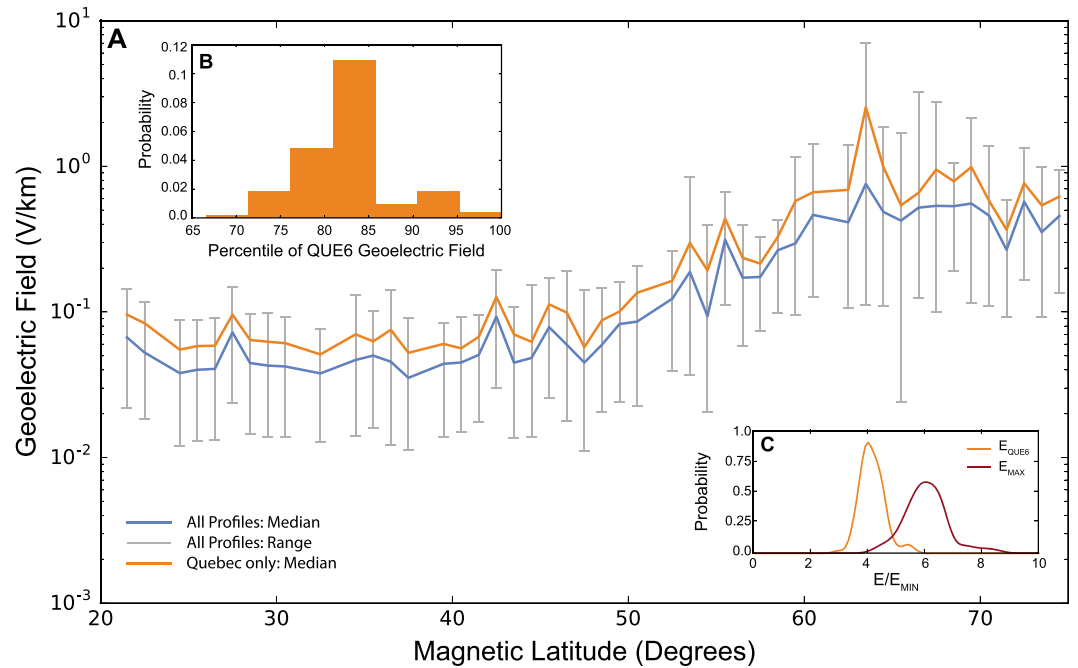


Figure 4. The effect of different conductivity profiles on calculated geoelectric fields for the 22–28 July 2004 storm time interval. (a) Geoelectric fields in 1° bins, with range plotted in gray, median plotted in blue, and median values for the QUE6 profile plotted in orange; (b) probability distribution of percentile at which values corresponding to the QUE6 profile occur; (c) probability distribution of the ratio of geoelectric field to smallest calculated value (from any profile) for the QUE6 profile (orange) and maximum calculated value from any profile (red). In Figure 4a, the absence of any gray lines in a latitudinal range indicates the absence of any available data at those latitudes. In Figures 4b and 4c, the probability distributions were calculated using kernel density estimation [Silverman, 1998].

for extreme storms. We should expect that the extreme storm fits would be accompanied by a larger degree of uncertainty, however. It is important to note that, as in section 3.1.1, a MADLOG(4) filter was applied before analysis in order to remove extreme outliers.

Our particular application of extreme value theory is known as the “block maxima method” [Gumbel, 1958]. In this approach, the maximum value of some quantity is evaluated within a standard “block” (oftentimes a year, but in our case, an individual storm which could last anywhere from a day to a week) and then the set of all these maxima is used to fit an extreme value distribution. Having thus obtained an analytical PDF, we can estimate the magnitude of GMD that would occur every 100 years [Wilks, 2006]. However, in order to make these estimations, it is necessary to first determine what value of the PDF corresponds to a “100 year” level.

We begin by noting that, in general, the expected frequency of occurrence for a GMD of amplitude A during a given type of storm is

$$f(A) = P(A|Dst)f(Dst) \quad (5)$$

where $P(A|Dst)$ is the probability of a perturbation of magnitude of at least A being observed during a storm of a given strength and $f(Dst)$ is the occurrence frequency for storms of a given strength.

Since the PDF is the derivative of the probability, the probability that a GMD will have a magnitude greater than or equal to A is given by

$$P(A|Dst) = \int_A^\infty \text{PDF}(x|Dst)dx = 1 - \int_{-\infty}^A \text{PDF}(x|Dst)dx \quad (6)$$

where the last equality shows that $P(A|Dst)$ is given by the complementary cumulative distribution function, also called the exceedance. Our next step is to determine the frequency with which different classes of storm occur.

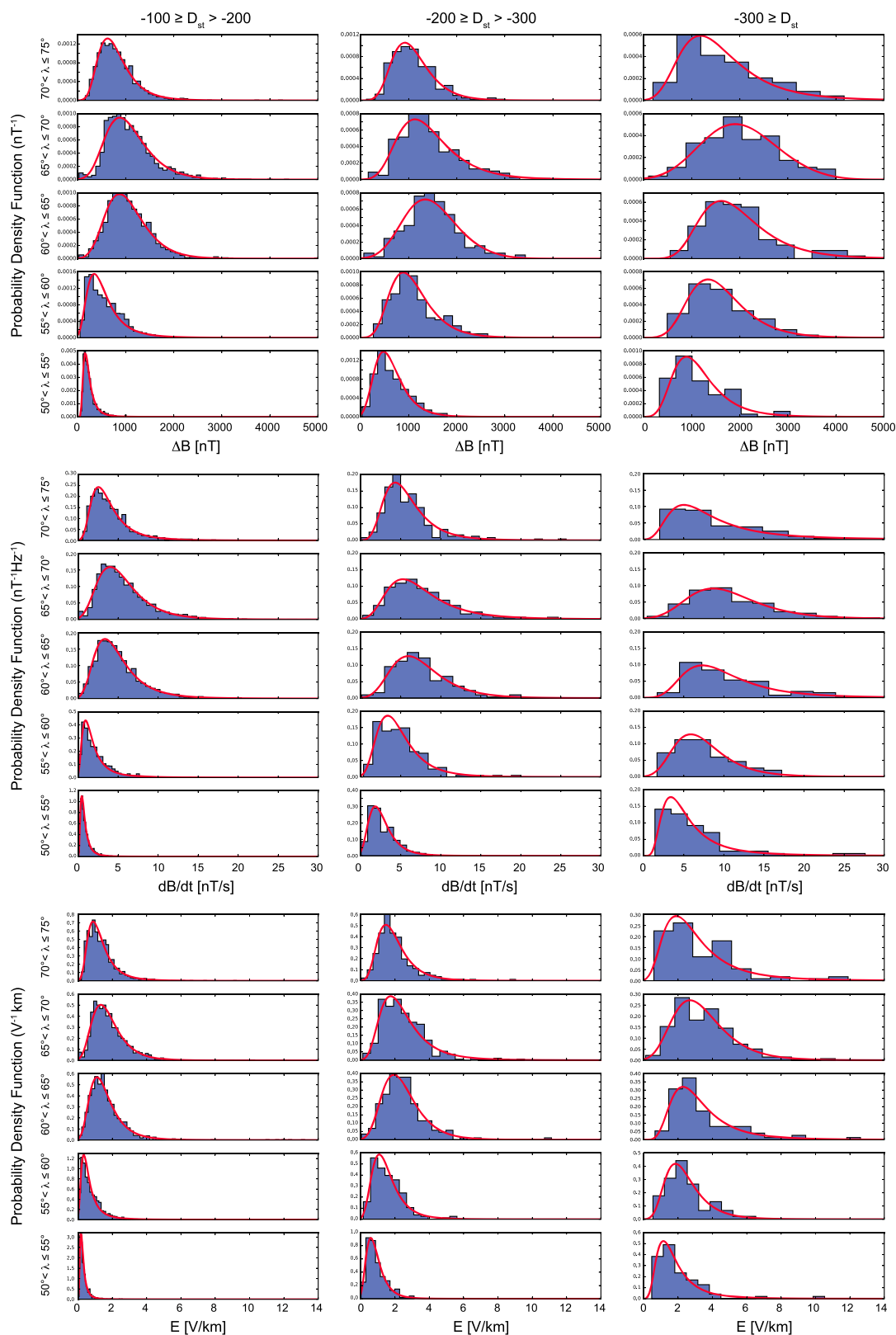


Figure 5. Variation of peak GMDs within latitudinal bins expressed as probability density function (PDF) of occurrence (this is related to the probability, $P(x)$, by $PDF(x) = dP(x)/dx$). Each column corresponds to a different strength of storm, while a row of plots corresponds to a particular 5° latitudinal bin (first to fifth rows are ΔB , sixth to tenth rows are B , and eleventh to fifteenth rows are E calculated using the QUE6 conductivity profile). In each plot, the normalized histogram (a common nonparametric PDF estimator) of GMD amplitudes is shown in blue and best fit GEVD for that data is shown in red.

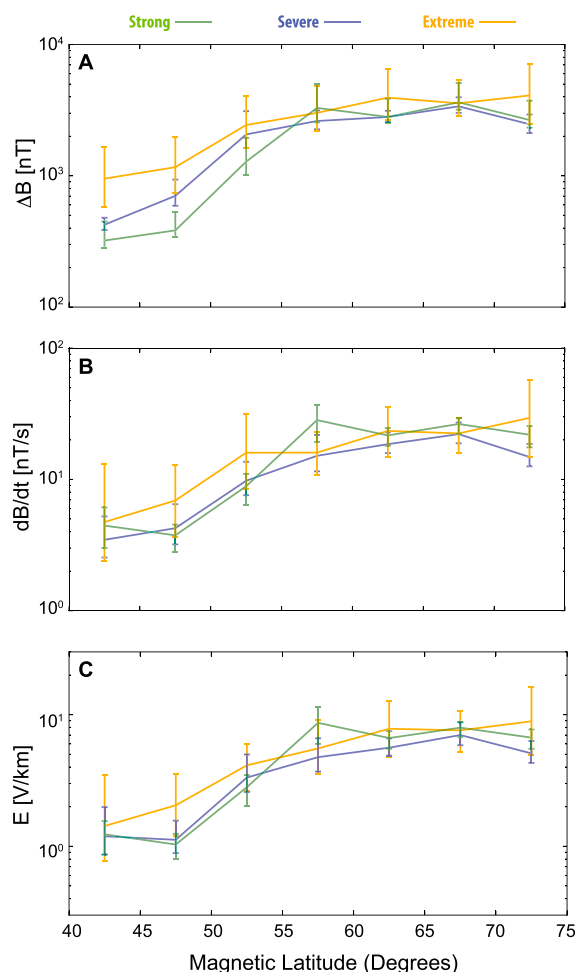


Figure 6. The magnitude of 1 in 100 year events for different types of GMD. (a) ΔB , (b) \dot{B} , and (c) E , calculated using the QUE6 conductivity profile. In each case, the values for strong storms are shown in green, values for severe storms are shown in blue, and values for extreme storms are shown in orange. Vertical error bars indicate the 95% confidence interval.

3.2.2. Storm Occurrence Frequency

We can estimate $f(Dst)$ over large time scales (i.e., over many solar cycles) using the average interval between storms in our 30 year data set: $f(Dst) = N(Dst)/30 \text{ yr}^{-1}$, where $N(Dst)$ is the number of storms of a given strength that occurred during the period of study. If we were to consider only our original data set, then these frequencies would be 6.0 yr^{-1} , 0.93 yr^{-1} , and 0.33 yr^{-1} . However, it may be the case that our 30 year interval is not a representative sample. To assess the representativeness our data set, we obtained Dst indices from all available years (1957–2015) and determined the number of geomagnetic storms of each class that occurred during each year. We then selected thirty years at random from this data set (with replacement) and totaled the number of storms from each class that occurred during the sample years. This sampling was repeated 1000 times, and the resultant data were used to find the median number of storms in each class along with a 95% confidence intervals. Following this procedure, we found that the median (95% CI) number of storms was 153 (117–189) strong, 25 (15–37) severe, and 10 (3–20) extreme. This analysis shows that the number of both severe and extreme storms in our data set is close to the median, and while the number of strong storms is somewhat higher than the median, it still lies within the confidence interval.

Based on the above CIs, strong storms are expected to occur with a frequency of $3.9\text{--}6.3 \text{ yr}^{-1}$, while severe storms should occur with a frequency of $0.5\text{--}1.23 \text{ yr}^{-1}$, and extreme storms should occur with a frequency of $0.1\text{--}0.67 \text{ yr}^{-1}$.

Table 4. 100 Year Peak GMD Amplitudes for Strong ($-100 \geq Dst > -200$ nT) Geomagnetic Storms at Different Latitudes^a

MLAT	ΔB (95% CI) (nT)	\dot{B} (95% CI) (nT/s)	E (95% CI) (V/km)
40°–45°	321 (284–448)	4.5 (3.0–6.1)	1.2 (0.9–1.6)
45°–50°	384 (344–530)	3.8 (2.8–4.5)	1.0 (0.8–1.2)
50°–55°	1282 (1008–1945)	8.9 (6.3–11.0)	2.8 (2.0–3.5)
55°–60°	3290 (2554–5032)	28.3 (19.3–37.0)	8.7 (6.0–11.5)
60°–65°	2808 (2524–3864)	21.6 (18.1–24.6)	6.6 (5.5–7.5)
65°–70°	3631 (3192–5089)	26.5 (22.3–29.3)	8.0 (6.8–8.8)
70°–75°	2661 (2332–3838)	21.9 (17.5–25.5)	6.7 (5.5–7.7)

^aElectric fields were calculated using the QUE6 conductivity profile.

3.2.3. Probabilistic Estimates of 100 Year GMDs

Using equation (5), we can calculate the magnitude of a 100 year GMD by choosing a storm occurrence frequency from section 3.2.2 and then using a fitted GEVD from section 3.2.1 to find the GMD magnitude that yields an exceedance equal to $f(A)/f(Dst)$.

As with our earlier median calculations, there is uncertainty in our GEVD fits that arise from the analysis of finite (sometimes small) data sets, and this uncertainty is compounded by the uncertain occurrence frequencies of different classes of storm. In order to assess the possible range of magnitudes that might correspond to 100 year GMDs, we again used bootstrap resampling as described in section 3.1.1 to calculate 100 year GMD values and their range of uncertainty. It should be noted that the quoted GMD values were calculated using the observed frequencies from our 30 year data set (e.g., 0.33 yr^{-1} for extreme storms) while the range of uncertainty ranges from the bottom of the 95% CI for the lowest frequency (e.g., 0.1 yr^{-1} for extreme storms) to the top of the 95% CI for the highest frequency (e.g., 0.67 yr^{-1} for extreme storms). Our estimated 100 year GMD magnitudes and their respective uncertainties are plotted in Figure 6, and 100 year GMD values for specific latitude ranges are summarized in Tables 4–6.

It is both interesting and important to note that the characteristics of the fit for ΔB differs greatly from those of \dot{B} and E . This difference was noted earlier in our discussion of the median peak GMDs. It is particularly interesting that the transition region is nearly twice as wide for \dot{B} and E than for ΔB , which supports our earlier suggestion that different phenomenologies may be responsible for the different types of GMD.

Our results are largely in agreement with previously cited results of Thomson *et al.* [2011], who estimated 100 year ΔB values of 2000–5000 nT and 100 year \dot{B} values of $16\text{--}66 \text{ nT/s}$ at $55^\circ \leq \lambda \leq 60^\circ$; from our data, we estimate $\Delta B \approx 2180\text{--}4819 \text{ nT}$ and $\dot{B} \approx 10.8\text{--}22.9 \text{ nT/s}$. The \dot{B} results from Thomson *et al.* [2011] suggest the possibility of larger-amplitude GMDs than our analysis, a discrepancy that is likely due to differences in data set and methodology. Methodologically, the points-over-threshold method used by Thomson *et al.* [2011] is specifically designed for analysis of values in a distribution's tail [Wilks, 2006] and may therefore provide a better estimate of very extreme values. As for the data set itself, longitudinally localized perturbations are not weighted as strongly in our data as they might be in that of Thomson *et al.* [2011] due to our inclusion of

Table 5. 100 Year Peak GMD Amplitudes for Severe ($-200 \geq Dst > -300$ nT) Geomagnetic Storms at Different Latitudes^a

MLAT	ΔB (95% CI) (nT)	\dot{B} (95% CI) (nT/s)	E (95% CI) (V/km)
40°–45°	424 (386–479)	3.5 (2.5–5.2)	1.2 (0.9–2.0)
45°–50°	703 (592–936)	4.3 (3.2–6.5)	1.1 (0.9–1.6)
50°–55°	2067 (1632–3107)	9.8 (7.6–13.6)	3.3 (2.6–5.0)
55°–60°	2615 (2260–3147)	15.1 (11.5–21.8)	4.8 (3.7–6.6)
60°–65°	2806 (2567–3130)	18.6 (15.9–22.8)	5.6 (4.9–6.6)
65°–70°	3382 (3018–3967)	22.1 (18.9–27.1)	7.0 (5.9–8.8)
70°–75°	2472 (2118–2931)	14.8 (12.6–18.7)	5.1 (4.3–6.3)

^aElectric fields were calculated using the QUE6 conductivity profile.

Table 6. 100 Year Peak GMD Amplitudes for Extreme ($-300 \geq Dst$) Geomagnetic Storms at Different Latitudes^a

MLAT	ΔB (95% CI) [nT]	\dot{B} (95% CI) [nT/s]	E (95% CI) [V/km]
40°–45°	951 (538–1156)	4.7 (2.4–13.2)	1.4 (0.8–3.5)
45°–50°	1164 (738–1987)	6.9 (3.6–12.9)	2.0 (1.2–3.5)
50°–55°	2436 (1622–4061)	15.9 (8.4–31.3)	4.1 (2.6–6.0)
55°–60°	3017 (2180–4819)	16.0 (10.8–22.9)	5.5 (3.5–9.1)
60°–65°	3941 (2682–6501)	23.4 (14.9–35.7)	7.8 (4.8–12.7)
65°–70°	3565 (2861–5337)	22.4 (15.8–29.5)	7.6 (5.2–10.6)
70°–75°	4094 (2499–7112)	29.4 (14.9–57.4)	8.9 (5.0–16.1)

^aElectric fields were calculated using the QUE6 conductivity profile.

observatories at all magnetic longitudes; also, the removal of extreme outliers via filtering could reduce the magnitude of estimated GMDs, since some real GMDs may have been rejected along with actual bad data. However, our maximum-likelihood fitting of GEVDs is primarily sensitive to values in the core of a distribution, so this should have a mitigating effect on the influence of rejected outliers.

The data in Tables 4–6 reveals an unexpected characteristic of GMDs: at latitudes above the transition region, the size of a 100 year GMD is essentially the same for each class of storm. Because the probability of a 100 year event depends on both the storm occurrence frequency and the probability of a given GMD magnitude occurring during such a storm, the relatively higher frequency of weaker storms (approximately 18:3:1 in our 30 year data set) compensates for the decreased probability of large-magnitude GMDs during those storms. The practical consequence of this observation is that at higher latitudes, dangerously large GMDs are just as likely (on average) to occur during strong, severe, and extreme storms and are therefore as much as 3 times more likely to occur than would be estimated based on a consideration of only extreme storms; at lower latitudes, only extreme storms are capable of producing these GMDs, so an analysis of extreme storms suffices to characterize the overall threat from large GMDs.

4. Conclusions

In this paper, we have examined the latitudinal distribution of peak GMD amplitudes during large ($Dst < -100$ nT) geomagnetic storms. Our study differs from previous efforts such as those of Thomson *et al.* [2011] or Ngwira *et al.* [2013] in the breadth of its data set and the levels of magnetic activity considered. With our large data set, we have been able to establish median latitudinal profiles of storm time GMDs and have identified characteristic Dst -dependent structure, showing how the region that is in danger of experiencing large GMDs moves equatorward with increasing storm intensity.

Using extreme value theory, we have also calculated 100 year GMD magnitudes as a function of both magnetic latitude and storm intensity, finding that dangerously large GMDs ($\dot{B} > 5$ nT/s, $E > 1$ V/km) can occur at latitudes as low as 45° during severe and extreme storms. Specifically, we have found that for the 45°–50° MLAT range (corresponding to much of the continental United States and central Europe), 100 year GMDs of $\Delta B = 738$ –1987 nT and $\dot{B} = 3.6$ –12.9 nT/s are expected during extreme storms, with the latter exceeding a well-recognized 5 nT/s threshold for induction hazards. Full results for 100 year GMDs across a range of latitudes are given in Tables 4–6.

Although we have found that extreme storms pose the greatest risk for lower latitudes, we have also found that this is not the case at high latitudes. For example, in the 55°–60° latitude range, the 100 year magnitude of \dot{B} is 19.3–37.0 nT/s for strong storms, 11.5–21.8 nT/s for severe storms, and 10.8–22.9 nT/s for extreme storms. These results indicate that accurate characterization of GMD hazards at these latitudes requires the consideration of more than just extreme storms, since less intense storms may actually produce larger GMDs.

Appendix A: The MADLOG(n) Filter

Because there exist some extreme and most likely unphysical outliers in any extended data set (due to various glitches, calibration errors, and processing issues), it is useful to have an automated and objective measure for removing these outliers. Our particular approach is to eliminate data whose logarithm is not within n median

absolute deviations (MADs) of the median of the logarithm of the data. Specifically, if we have a data set \mathbf{x} , we define the MADLOG as

$$\text{MADLOG} = \langle |\log(\mathbf{x}) - \langle \log(\mathbf{x}) \rangle| \rangle \quad (\text{A1})$$

where $\langle \dots \rangle$ indicates the median of the enclosed quantity and $|\dots|$ indicates the absolute value; based on this definition, the MADLOG(n) filter then removes any data that do not satisfy

$$-n \leq \frac{\log(\mathbf{x}) - \langle \log(\mathbf{x}) \rangle}{\text{MADLOG}} \leq n \quad (\text{A2})$$

Acknowledgments

We would like to thank Michael Rivera and Scott Backhaus of the Information Systems and Modeling group at Los Alamos National Laboratory for motivating this study as well as for their input and feedback during the preparation of this report. This research was supported by the SHIELDS project, a LANL/Laboratory Directed Research and Development (LDRD) Program funded by the U.S. Department of Energy. In addition, the Department of Homeland Security sponsored the production of this material under the Department of Energy contract for the management and operation of Los Alamos National Laboratory. S.K.M. was partially supported by LANL LDRD award 20150127ER. The *Dst* geomagnetic index was obtained from the World Data Center C2 for Geomagnetism in Kyoto. Magnetometer data and derived indices were obtained from the SuperMAG collaboration web site, <http://supermag.jhuapl.edu>. For the ground magnetometer data we gratefully acknowledge Intermagnet; USGS, Jeffrey J. Love; CARISMA, Ian Mann; CANMOS; the S-RAMP database, K. Yumoto, and K. Shiokawa; The SPIDR database; AARI, Oleg Troshichev; the MACCS program, M. Engebretson, Geomagnetism Unit of the Geological Survey of Canada; GIMA; MEASURE, UCLA IGPP, and Florida Institute of Technology; SAMBA, Eftyhia Zesta; 210 Chain, K. Yumoto; SAMNET, Farideh Honary; the institutes who maintain the IMAGE magnetometer array, Eija Tanskanen; PENGUIN; AUTUMN, PI Martin Connors; DTU Space, Juergen Matzka; South Pole and McMurdo Magnetometer, PI's Louis J. Lanzarotti and Alan T. Weatherwax; ICESAR; RAPIDMAG; PENGUIN; British Antarctic Survey; McMac, Peter Chi; BGS, Susan Macmillan; Pushkov Institute of Terrestrial Magnetism, Ionosphere and Radio Wave Propagation (IZMIRAN); GFZ, Juergen Matzka; MFGI, B. Heilig; IGFPA, J. Reda; University of LAquila, M. Vellante; and SuperMAG, Jesper W. Gjerloev. Sunspot numbers were obtained from the WDC-SILSO, Royal Observatory of Belgium, Brussels. Analysis of the data presented in this study made use of SpacePy software package, available at <http://sourceforge.net/p/spacepy>.

For our data set, we have found that that $n = 4$ was effective at removing suspect data while leaving the bulk of the data untouched.

References

- Ádám, A., E. Prácer, and V. Wesztergom (2012), Estimation of the electric resistivity distribution (EURHOM) in the European lithosphere in the frame of the EURISGIC WP2 project, *Acta Geod. Geophys. Hung.*, **47**(4), 377–387, doi:10.1556/AGEod.47.2012.4.1.
- Boteler, D. H. (2001), Assessment of geomagnetic hazard to power systems in Canada, *Nat. Hazards*, **23**, 101–120, doi:10.1023/A:1011194414259.
- Boteler, D. H. (2015), The evolution of the Québec earth models used to model geomagnetically induced currents, *IEEE Trans. Power Delivery*, **30**(5), 2171–2178, doi:10.1109/TPWRD.2014.2379260.
- Boteler, D. H., R. J. Pirjola, and H. Nevanlinna (1998), The effects of geomagnetic disturbances on electrical systems at the Earth's surface, *Adv. Space Res.*, **22**(1), 17–27, doi:10.1016/S0273-1177(97)01096-X.
- Cagniard, L. (1953), Basic theory of the magneto-telluric methods of geophysical prospecting, *Geophysics*, **18**(3), 605–635.
- Danskin, D. W., and S. I. Lotz (2015), Analysis of geomagnetic hourly ranges, *Space Weather*, **13**, 458–468, doi:10.1002/2015SW001184.
- Dyson, F. (2004), Turning points: A meeting with Enrico Fermi, *Nature*, **427**, 297, doi:10.1038/427297a.
- Efron, B., and R. Tibshirani (1986), Bootstrap methods for standard errors, confidence intervals, and other measures of statistical accuracy, *Stat. Sci.*, **1**(1), 54–75.
- Eroshenko, E. A., A. V. Belov, D. H. Boteler, S. P. Gaidash, S. L. Lobokov, R. Pirjola, and L. Trichtchenko (2010), Effects of strong geomagnetic storms on Northern railways in Russia, *Adv. Space Res.*, **46**(9), 1102–1110.
- Fernberg, P. (2012), One-dimensional Earth resistivity models for selected areas of continental United States and Alaska, *EPRI Rep. 1026430*, [Available at <http://www.epri.com/abstracts/Pages/ProductAbstract.aspx?Productid=0000000001026430>, Accessed 20 July 2016.]
- Freedman, D., and P. Diaconis (1981), On the histogram as a density estimator: L2 theory, *Z. Wahrscheinlichkeit*, **57**, 453–476.
- Ganushkina, N. Y., et al. (2015), Defining and resolving current systems in geospace, *Ann. Geophys.*, **33**, 1369–1402, doi:10.5194/angeo-33-1369-2015.
- Ghil, M., et al. (2011), Extreme events: Dynamics, statistics and prediction, *Nonlinear Processes Geophys.*, **18**, 295–350, doi:10.5194/npg-18-295-2011.
- Gjerloev, J. W. (2012), The SuperMAG data processing technique, *J. Geophys. Res.*, **117**, A09213, doi:10.1029/2012JA017683.
- Gonzalez, W. D., J. A. Joselyn, Y. Kamide, H. W. Kroehl, G. Rostoker, B. T. Tsurutani, and V. M. Vasyliunas (1994), What is a geomagnetic storm, *J. Geophys. Res.*, **99**(A4), 5771–5792, doi:10.1029/93JA02867.
- Gumbel, E. J. (1958), *Statistics of Extremes*, Columbia Univ. Press, New York.
- Guo, J., H. Liu, X. Feng, T. I. Pulkkinen, E. I. Tanskanen, C. Liu, D. Zhong, and Y. Wang (2014), MLT and seasonal dependence of auroral electrojets: IMAGE magnetometer network observations, *J. Geophys. Res. Space Physics*, **119**, 3179–3188, doi:10.1002/2014JA019843.
- Halford, A. J., B. J. Fraser, and S. K. Morley (2010), EMIC wave activity during geomagnetic storm and nonstorm periods: CRRES results, *J. Geophys. Res.*, **115**, A12248, doi:10.1029/2010JA015716X.
- Hapgood, M. (2010), Space Weather: Its impact on Earth and implications for business, Lloyds of London. [Available at <https://www.lloyds.com/news-and-insight/risk-insight/library/natural-environment/space-weather>, Accessed 16 May 2016.]
- Hapgood, M. A. (1992), Space physics coordinate transforms: A user guide, *Planet. Space Sci.*, **40**(5), 711–717.
- Kamide, Y., and S. Kokubun (1996), Two-component auroral electrojet: Importance for substorm studies, *J. Geophys. Res.*, **101**(A6), 13,027–13,046.
- Kappenman, J. G. (2003), Storm sudden commencement events and the associated geomagnetically induced current risks to ground-based systems at low-latitude and midlatitude locations, *Space Weather*, **1**(3), 1016, doi:10.1029/2003SW000009.
- Le, G., C. T. Russell, and K. Takahashi (2004), Morphology of the ring current derived from magnetic field observations, *Ann. Geophys.*, **22**, 1267–1295.
- Limpert, E. (2001), Log-normal distributions across the Sciences: Keys and clues, *BioScience*, **51**(5), 341–352.
- Loewe, C. A., and G. W. Pröls (1997), Classification and mean behavior of geomagnetic storms, *J. Geophys. Res.*, **102**(A7), 14,209–14,213.
- Love, J. J. (2013), An international network of magnetic observatories, *Eos Trans. AGU*, **94**(42), 373–384.
- Love, J. J., E. J. Rigler, A. Pulkkinen, and P. Ridley (2015), On the log-normality of historical magnetic storm intensity statistics: Implications for extreme-event probabilities, *Geophys. Res. Lett.*, **42**, 6544–6553, doi:10.1002/2015GL064842.
- Marshall, R. A., C. L. Waters, and M. D. Sciffer (2010), Spectral analysis of pipe-to-soil potentials with variations of the Earth's magnetic field in the Australian region, *Space Weather*, **8**, S05002, doi:10.1029/2009SW000553.
- Molinski, T. S., W. E. Feero, and B. L. Damsky (2000), Shielding grids from solar storms, *IEEE Spectr.*, **37**(11), 55–60, doi:10.1109/6.880955.
- NERC GMD Task Force (2015), *TPL-007-1 Transmission System Planned Performance for Geomagnetic Disturbance Events*, Natl. Energy Reliab. Corp. [Available at <http://www.nerc.com/pa/Stand/Pages/Project-2013-03-Geomagnetic-Disturbance-Mitigation.aspx>, Accessed 20 July 2016.]
- National Research Council Committee on the Societal and Economic Impacts of Severe Space Weather Events (2008), *Severe Space Weather Events—Understanding Societal and Economic Impacts: A Workshop Report*, Natl. Acad. Press, Washington, D. C., doi:10.17226/12507.
- Newell, P. T., and J. W. Gjerloev (2012), SuperMAG-based partial ring current indices, *J. Geophys. Res.*, **117**, A05215, doi:10.1029/2012JA017586.

- Ngwira, C. N., A. Pulkkinen, F. D. Wilder, and G. Crowley (2013), Extended study of extreme geoelectric field event scenarios for geomagnetically induced current applications, *Space Weather*, *11*, 121–131, doi:10.1002/swe.20021.
- Ngwira, C. N., A. Pulkkinen, E. Bernabeu, J. Eichner, A. Viljanen, and G. Crowley (2015), Characteristics of extreme geoelectric fields and their possible causes: Localized peak enhancements, *Geophys. Res. Lett.*, *42*, 6916–6921, doi:10.1002/2015GL065061.
- Ptitsyna, N. G., V. V. Kasinskii, G. Villoresi, N. N. Lyahov, L. I. Dorman, and N. Lucci (2008), Geomagnetic effects on mid-latitude railways: A statistical study of anomalies in the operation of signaling and train control equipment on the East-Siberian Railway, *Adv. Space Res.*, *42*(9), 1510–1514.
- Press, W. H., S. A. Teukolsky, W. T. Vetterling, and B. P. Flannery (1992), *Numerical Recipes in Fortran*, 2nd ed., Cambridge Univ. Press, New York.
- Pulkkinen, A., E. Bernabeu, J. Eichner, C. Beggan, and A. W. P. Thomson (2012), Generation of 100-year geomagnetically induced current scenarios, *Space Weather*, *10*, S04003, doi:10.1029/2011SW000750.
- Reay, S. J., W. Allen, O. Ballie, J. Bowe, E. Clarke, V. Lesur, and S. Macmillan (2005), Space weather effects on drilling accuracy in the North Sea, *Ann. Geophys.*, *23*, 3081–3088.
- Rostoker, G., and T. Phan (1986), Variation of auroral electrojet spatial location as a function of the level of magnetospheric activity, *J. Geophys. Res.*, *91*(A2), 1716–1722.
- Schulz, M. (1997), Direct influence of ring current on auroral oval diameter, *J. Geophys. Res.*, *102*(A7), 14,149–14,154.
- Sckopke, N. (1966), A general relation between the energy of trapped particles and the disturbance field near the Earth, *J. Geophys. Res.*, *71*(13), 3125–3130.
- Shinbori, A., Y. Tsuji, T. Kikuchi, T. Araki, and S. Watari (2009), Magnetic latitude and local time dependence of the amplitude of geomagnetic sudden commencements, *J. Geophys. Res.*, *114*, A04217, doi:10.1029/2008JA013871.
- Silverman, B. W. (1998), *Density Estimation for Statistics and Data Analysis*, Chapman and Hall/CRC, London.
- Starkov, G. V., and Y. I. Feldstein (1967), Variations of auroral oval boundaries, *Geomagn. Aeron.*, *7*, 62–71.
- Thomson, A. W., E. B. Dawson, and S. J. Reay (2011), Quantifying extreme behavior in geomagnetic activity, *Space Weather*, *9*, S10001, doi:10.1029/2011SW000696.
- Tomita, S., et al. (2011), Magnetic local time dependence of geomagnetic disturbances contributing to the AU and AL indices, *Ann. Geophys.*, *29*, 673–678.
- Viljanen, A., H. Nevanlinna, K. Pajunpää, and A. Pulkkinen (2001), Time derivative of the horizontal geomagnetic field as an activity indicator, *Ann. Geophys.*, *19*, 1107–1118.
- Viljanen, A., A. Koistinen, K. Pajunpää, R. Pirjola, P. Posio, and A. Pulkkinen (2010), Recordings of geomagnetically induced currents in the Finnish natural gas pipeline—Summary of an 11-year period, *Geophysica*, *46*(1–2), 59–67.
- Viljanen, A., R. Pirjola, M. Wik, A. Ådåm, E. Præcser, Y. Sakharov, and J. Katkalov (2012), Continental scale modeling of geomagnetically induced currents, *J. Space Weather Space Clim.*, *2*, A17, doi:10.1051/swsc/2012017.
- Viljanen, A., R. Pirjola, E. Præcser, J. Katkalov, and M. Wik (2014), Geomagnetically induced currents in Europe, *J. Space Weather Space Clim.*, *4*, A09, doi:10.1051/swsc/2014006.
- Wait, J. R. (1958), Transmission and reflection of electromagnetic waves in the presence of stratified media, *J. Res. Nat. Bur. Stand.*, *61*(3), 205–232.
- Watermann, J., O. Rasmussen, P. Stauning, and H. Gleisner (2006), Temporal versus spatial geomagnetic variations along the west coast of Greenland, *Adv. Space Res.*, *37*, 1163–1168, doi:10.1016/j.asr.2005.08.019.
- Wei, L. S., N. Homeier, and J. Gannon (2013), Surface electric fields for North America during historical geomagnetic storms, *Space Weather*, *11*, 451–462, doi:10.1002/swe.20073.
- Wilks, D. S. (2006), *Statistical Methods in the Atmospheric Sciences*, 2nd ed., Academic Press, New York.